Stacking-dependent topological magnons in bilayer CrI_3

Maarten Soenen [1], Cihan Bacaksiz [1,2,3], Raí M. Menezes [1], and Milorad V. Milošević [1,4,*]

[1]*Department of Physics & NANOlab Center of Excellence, University of Antwerp, Groenenborgerlaan 171, B-2020 Antwerp, Belgium*

[2]*Bremen Center for Computational Material Science (BCCMS), Bremen D-28359, Germany*

[3]*Computational Biotechnology, RWTH Aachen University, Worringerweg 3, 52074 Aachen, Germany*

[4]*Instituto de Física, Universidade Federal de Mato Grosso, Cuiabá, Mato Grosso 78060-900, Brazil*

(Received 8 December 2022; revised 30 January 2023; accepted 15 February 2023; published 28 February 2023)

Motivated by the potential of atomically thin magnets towards achieving tunable high-frequency magnonics, we detail the spin-wave dispersion of bilayer CrI_3. We demonstrate that the magnonic behavior of the bilayer strongly depends on its stacking configuration and the interlayer magnetic ordering, where a topological band gap opens in the dispersion caused by the Dzyaloshinskii-Moriya and Kitaev interactions, classifying bilayer CrI_3 as a topological magnon insulator. We further reveal that both the size and the topology of the band gap in a CrI_3 bilayer with an antiferromagnetic interlayer ordering are tunable by an external magnetic field.

DOI: 10.1103/PhysRevMaterials.7.024421

I. INTRODUCTION

Emergent two-dimensional (2D) magnetic materials [1] provide an exciting platform to study collective spin excitations, i.e., magnons. CrI_3, the archetypal 2D van der Waals (vdW) ferromagnet [2], has recently been suggested to host magnon modes in the highly sought-after terahertz regime [3–5], showing promise for the development of faster and more energy-efficient data processing applications [6]. Moreover, due to the 2D nature of the material, its spin-wave properties are highly susceptible to tuning, e.g., by strain, buckling, defect engineering, gating, and/or vdW heterostructuring [5].

Recently, several bulk materials, including $CrBr_3$ [7], CrI_3 [8,9], $CrSiTe_3$ [10], and $CrGeTe_3$ [10], have been identified as *topological magnon insulators* (TMIs), characterized by bulk magnon bands with a gap at the Dirac point and topologically protected edge states. The magnonic band gap is attributed to the antisymmetric exchange interaction—more often called the Dzyaloshinskii-Moriya interaction (DMI) [11,12]—arising from the lack of inversion symmetry between next-nearest-neighboring (NNN) Cr atoms. In contrast, bulk $CrCl_3$ [13,14], where the DMI is weak, is classified as a *magnon Dirac material* (MDM), characterized by a Dirac point in the dispersion, showing a linear band crossing at the Brillouin zone edge.

However, it remains an open question whether the topological features of the aforementioned materials will persist down to the monolayer limit. Early theoretical work suggested that honeycomb ferromagnetic (FM) monolayers could be classified as either MDMs or TMIs depending on whether any NNN DMI is present in the material [15–20]. Nonetheless, recent work identified Kitaev interactions as an alternative mechanism potentially able to open a topological band gap in FM honeycomb materials [21,22], suggesting that the absence of DMI is not the sole criterion for predicting the topological properties of such materials. Similarly, in magnetic honeycomb bilayers, a DMI-induced topological behavior of magnons is predicted [20,23–25], including the formation of Dirac magnon nodal-line loops [23] and the opening of a topological band gap, which contributes to a magnon Hall effect and a spin Nernst effect [20,24,25].

Several recent works [26–29] attempted to characterize the magnonics of monolayer CrI_3 using *ab initio* calculations and demonstrated the appearance of a small, possibly topological, band gap caused by the spin-orbit coupling (SOC), suggesting that the material is a TMI. However, more work is required before full understanding of the magnonics in CrI_3 is achieved. In this paper, we deploy a multiscale approach, combining *ab initio* calculations with numerical simulations based on a Heisenberg model and linear spin-wave theory, to characterize the magnonic properties of CrI_3 monolayers and bilayers, reveal the topological magnon modes present in these systems, and show that the (topological) magnonic properties of the bilayer are strongly affected by its stacking order and its interlayer magnetic ordering.

The paper is organized as follows. In Sec. II, we describe the computational methodology used in this paper. We discuss the Heisenberg Hamiltonian that models the magnetic interactions in CrI_3, explain how the parameters that characterize this Hamiltonian will be derived from first principles, and, finally, sketch how the spin-wave dispersion is computed. Subsequently, in Sec. III, we apply this methodology to monolayer CrI_3, confirming the presence of a small topological band gap with nonzero Chern numbers in the material's spin-wave dispersion. Afterwards, in Sec. IV, we consider bilayer CrI_3 in three different stacking orders, each exhibiting significantly different magnonic behavior. Specifically, we investigate the AA stacking and AB stacking (rhombohedral) discussed in the literature [20,23,24], as well as the experimentally very relevant AB′ stacking (monoclinic), the spin waves of which have—to the best of our knowledge—not been theoretically investigated to date. We find that all three stacking versions

*milorad.milosevic@uantwerpen.be

of bilayer CrI_3 exhibit either FM or antiferromagnetic (AFM) interlayer ordering, with intralayer ferromagnetism. In the case of a FM interlayer ordering, we observe a band gap in the spin-wave dispersion with stacking-dependent topological properties. We attribute the origin of the gap to a combination of DMI and Kitaev interactions that are modulated by the stacking order. Furthermore, we show a significant influence of the interlayer magnetic ordering on the resulting magnonic behavior. Specifically, the topological nature of the bands becomes trivial in AFM-ordered bilayers. Additionally, we show that magnonic dispersion of AFM-ordered bilayers is susceptible to tuning by an external magnetic field, lifting the degeneracy between branches, which decreases the size of the magnonic band gap and leads to a nontrivial topology of the bands in the AB′ stacking, or introduces nodal-line loops in the AA-stacking case. Finally, Sec. V summarizes our findings and gives an outlook on some future challenges and opportunities within the field.

II. COMPUTATIONAL METHODOLOGY

We model the magnetic interactions of the system under study using a Heisenberg spin Hamiltonian of the following form:

$$\hat{\mathcal{H}} = \frac{1}{2}\sum_{i,j}\hat{\mathbf{S}}_i\mathcal{J}_{ij}\hat{\mathbf{S}}_j + \sum_i \hat{\mathbf{S}}_i\mathcal{A}_{ii}\hat{\mathbf{S}}_i + \mu_{\mathrm{B}}\sum_i \mathbf{B}\cdot g_i\hat{\mathbf{S}}_i, \quad (1)$$

in which the spins are three-dimensional (3D) vectors $\hat{\mathbf{S}}_i = (\hat{S}_i^x, \hat{S}_i^y, \hat{S}_i^z)$ expressed in Cartesian coordinates. The first and second terms of this Hamiltonian describe the exchange interaction and the single-ion anisotropy (SIA), respectively, which are characterized by the 3×3 matrices $\mathcal{J}_{ij}$ and $\mathcal{A}_{ii}$. The DMI is characterized by a vector $\mathbf{D}_{ij}$ with components that can be calculated from the off-diagonal elements of the exchange matrix as $D_{ij}^x = \frac{1}{2}(\mathcal{J}_{ij}^{yz} - \mathcal{J}_{ij}^{zy})$, $D_{ij}^y = \frac{1}{2}(\mathcal{J}_{ij}^{zx} - \mathcal{J}_{ij}^{xz})$, and $D_{ij}^z = \frac{1}{2}(\mathcal{J}_{ij}^{xy} - \mathcal{J}_{ij}^{yx})$ [30,31]. Notice that $\mathbf{D}_{ij} = \nu_{ij}|\mathbf{D}_{ij}|$ with $\nu_{ij} = -\nu_{ji} = \pm 1$, where the sign of the latter depends on the hopping direction of the considered spin pair. The exchange term is now written as

$$\hat{\mathcal{H}}_{\mathrm{ex}} = \frac{1}{2}\sum_{i,j}\left[\sum_{\alpha'} J_{ij}^{\alpha'}\hat{S}_i^{\alpha'}\hat{S}_j^{\alpha'} + \mathbf{D}_{ij}(\hat{\mathbf{S}}_i\times\hat{\mathbf{S}}_j)\right], \quad (2)$$

with $\alpha' = \{\alpha, \beta, \gamma\}$ being the local eigenbases that diagonalize the symmetric part of the exchange matrices. To consider the exchange anisotropy, we define the Kitaev constant as $K_{ij} = J_{ij}^{\gamma} - J_{ij}$ with $J_{ij} = (J_{ij}^{\alpha} + J_{ij}^{\beta})/2$ being the isotropic exchange constant [32], leading to the following expression for the exchange Hamiltonian:

$$\hat{\mathcal{H}}_{\mathrm{ex}} = \frac{1}{2}\sum_{i,j}\left[J_{ij}\hat{\mathbf{S}}_i\cdot\hat{\mathbf{S}}_j + K_{ij}\hat{S}_i^{\gamma}\hat{S}_j^{\gamma} + \mathbf{D}_{ij}(\hat{\mathbf{S}}_i\times\hat{\mathbf{S}}_j)\right].$$

The symmetric SIA matrix $\mathcal{A}_{ii}$ accounts for the interaction of the magnetic orbitals with the surrounding crystal field and contributes to the magnetic anisotropy of the material. In crystals with a threefold, fourfold, or sixfold rotational symmetry around the out-of-plane axis, most elements of the matrix are redundant, and the SIA can be characterized by a single parameter $\mathcal{A}_{ii}^{zz}$ instead of the full SIA matrix [30,31]. The last term of Eq. (1) accounts for the Zeeman interaction when applying an external magnetic field $\mathbf{B}$, where $g_i \approx 2$ is the g factor and μ_{B} is the Bohr magneton. In CrI_3, the magnetic dipole-dipole interaction is expected to be small in comparison to its out-of-plane magnetic anisotropy and will therefore not be included in the Heisenberg Hamiltonian [5]. Finally, also notice that CrI_3 has a magnetic moment of $\mu = 3\ \mu_{\mathrm{B}}$ per chromium atom and thus a spin of $S = \frac{3}{2}$.

To obtain the elements of the exchange and SIA matrices, we use the four-state energy mapping (4SM) methodology [30,31], in which we calculate the energies of several spin configurations of the system from first principles using density functional theory (DFT) and map these energies on their corresponding Heisenberg Hamiltonians, setting up a system of equations from which the magnetic parameters can be derived. The implementation of the needed DFT calculations is thoroughly discussed in Sec. SI of the Supplemental Material [33].

The spin-wave dispersion relations are calculated numerically using the open-source code SPINW [43], in which we have implemented our Heisenberg Hamiltonian. This code is based on linear spin-wave theory, which is a good approximation assuming that spin fluctuations are small. This condition is comfortably satisfied at low temperatures, significantly below the critical temperature (Curie or Néel) of the long-range magnetic order at hand. Numerical diagonalization of the Heisenberg Hamiltonian in reciprocal space yields the spin-wave dispersion.

III. MONOLAYER

A. Crystal structure and magnetic parameters

The crystal structure of monolayer CrI_3 is depicted in Figs. 1(a) and 1(e). Monolayer CrI_3 comprises one honeycomb layer of chromium atoms sandwiched between two layers of iodine atoms, where each chromium atom is octahedrally coordinated with six iodine atoms, and each iodine atom connects two chromium atoms through an $\approx 90^\circ$ Cr-I-Cr bond. After structural relaxation using DFT, we find an in-plane lattice constant of $a = 6.919$ Å.

To characterize the magnetic interactions in CrI_3, we perform a 4SM analysis in order to obtain the elements of the exchange and SIA matrices. In Table I, we report the average nearest-neighbor (NN) and next-nearest-neighbor (NNN) intralayer exchange, Kitaev, and DMI parameters for monolayer CrI_3. A full summary of the exchange parameters of all the individual pairs can be found in Sec. SIV of the Supplemental Material [33]. Notice that third-nearest-neighbor (3NN) and higher-order exchange terms are not taken into account as their influence on the spin-wave dispersion is negligible [33].

From the calculated parameters, it becomes clear that both the NN and the NNN exchange interactions are anisotropic and FM, with the NN one delivering the dominant contribution. In agreement with the literature [45,46], we find that the material's out-of-plane magnetic anisotropy originates mainly from the NN exchange anisotropy, with a smaller contribution of $\langle\mathcal{A}_{ii}^{zz}\rangle = -0.08$ meV due to the SIA. The SIA is characterized by a single parameter owing to the material's threefold rotational symmetry. The NN interactions deliver no

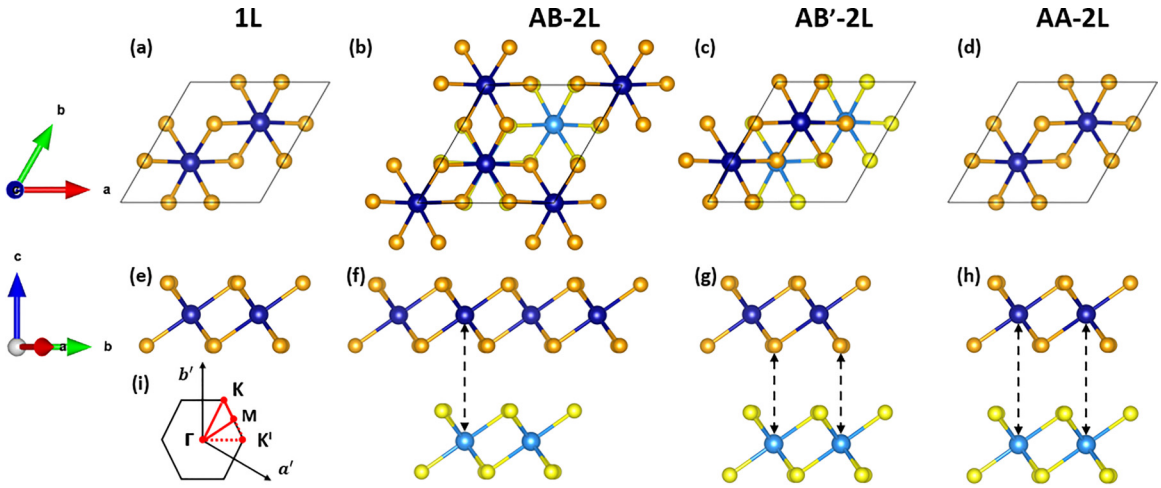

FIG. 1. Crystal structure of monolayer and bilayer CrI_3. Top view [(a)–(d)] and side view [(e)–(h)] of monolayer (1L) CrI_3 [(a) and (e)] and bilayer (2L) CrI_3 with an AB stacking [(b) and (f)], AB′ stacking [(c) and (g)], and AA stacking [(d) and (h)]. For the sake of clarity, atoms of the same type are assigned a different color in the top and the bottom layer. In the bottom (top) layer, the chromium and iodine atoms are depicted with blue (dark blue) and yellow (orange) spheres, respectively. The unit cell is marked with a solid black line. All crystal structures were plotted using VESTA [44]. (i) depicts the corresponding first Brillouin zone and high-symmetry points for 2D systems with a hexagonal lattice.

net contribution to the DMI since the inversion symmetry of the material is upheld. However, this symmetry is not present between NNN sites, resulting in a small yet nonzero DMI. Notice that, in CrI_3, the DMI, the Kitaev interaction, and the SIA all originate from the large SOC arising due to the heavy iodine ligands [32,45,46].

B. Spin-wave dispersion

Figure 2(a) depicts the spin-wave dispersion of monolayer CrI_3 along the high-symmetry directions of the first Brillouin zone. Two distinct branches are present, as is expected for a unit cell containing two magnetic atoms. At the Γ point, the dispersion shows a Goldstone gap due to the magnetic anisotropy of the material. The gap has a size of $\Delta_\Gamma = 0.43$ meV and is an essential prerequisite for the existence of long-range magnetic order in 2D systems at finite temperatures [45]. The latter can be seen by considering the total number of magnons excited at temperature T, which is given by

$$N = \int \frac{\mathcal{D}(\omega_{\mathbf{k}})}{e^{\hbar\omega_{\mathbf{k}}/k_B T} - 1} d\omega_{\mathbf{k}}, \tag{3}$$

where $\mathcal{D}(\omega_{\mathbf{k}})$ is the magnon density of states, which is constant in 2D, k_B is the Boltzmann constant, and $\omega_{\mathbf{k}}$ are the spin-wave frequencies. When the dispersion is gapless, i.e., in the absence of magnetic anisotropy, this integral will diverge for $\omega_{\mathbf{k}} = 0$, preventing long-range 2D magnetic order at nonzero temperature in accordance with the Mermin-Wagner theorem [47].

TABLE I. Magnetic parameters for monolayer CrI_3. Summary of the most important magnetic parameters in monolayer CrI_3, including the exchange and Kitaev constants J_{ij} and K_{ij} and the size of the DMI vectors $|\mathbf{D}_{ij}|$. Values are given in meV.

J_{NN}	K_{NN}	$\lvert\mathbf{D}_{\mathrm{NN}}\rvert$	J_{NNN}	K_{NNN}	$\lvert\mathbf{D}_{\mathrm{NNN}}\rvert$
−4.35	1.49	0.00	−0.74	0.17	0.06

The lower energy "acoustic" branch displays quadratic behavior near the Γ point and is associated with an in-phase precession of the spins [see Fig. 2(b)], while the higher-energy "optical" branch is associated with an out-of-phase precession of the spins [see Fig. 2(c)]. The two branches meet at the K point, where they are separated by a small band gap of $\Delta_K = 0.15$ meV. At the K' point we find a gap of the same size, since the sublattice symmetry is upheld. The origin of this Dirac gap is partially attributed to the NNN DMI and partially to the Kitaev interactions. The determined band gap is smaller than but comparable in size to those given in Ref. [27] and Ref. [29], which report band gaps of 0.30 and 0.47 meV, respectively. Differences might be attributed to the use of different methodologies and *ab initio* parameters. However, these theoretically predicted band gaps all differ significantly from the experimentally observed one of 2.8 meV in bulk CrI_3 [9] (currently, there are no measurements for monolayer CrI_3 available). Note that some recent work [26] found a band gap of 2 meV, which is significantly closer to the experimental value. The origin of this discrepancy between theory and experiment is still open to debate; however, magnon-phonon interactions [28]—whose effect is not captured in our model—are suggested to be responsible for the enhancement of the band gap. Despite the quantitative differences, our results show a good qualitative agreement with the earlier-mentioned works.

At the K point ($\lambda = 3a/2$), the spins will precess at 120° angles to each other, as is shown in Figs. 2(d) and 2(e) for the lower and higher branch, respectively. If one only considered a purely isotropic NN exchange, these two states would be energetically degenerate resulting in a Dirac point. However, introducing Kitaev interactions and/or a NNN exchange term which includes a nonzero DMI component lifts

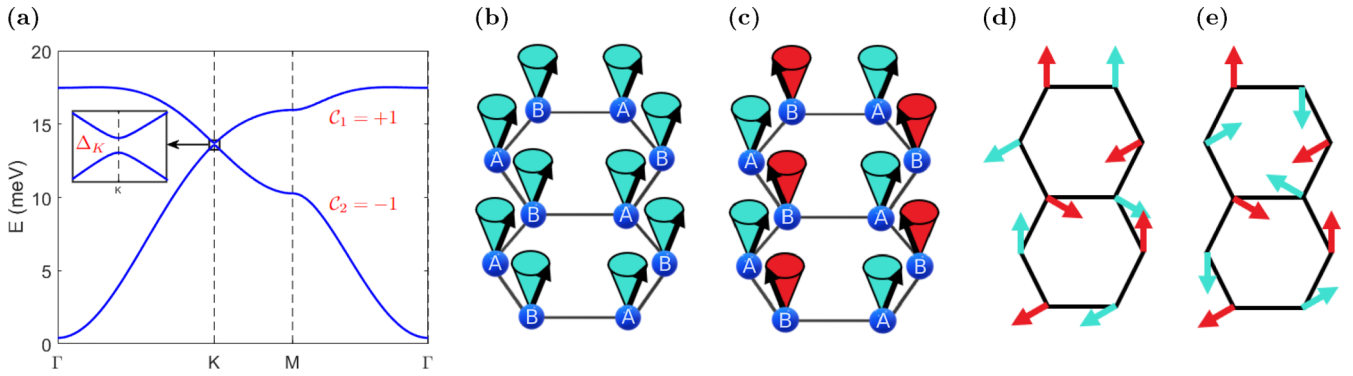

FIG. 2. Spin-wave dispersion of monolayer CrI_3. (a) Spin-wave dispersion along the high-symmetry directions of the first Brillouin zone. A small Dirac gap of $\Delta_K = 0.15$ meV is present at the K point. Corresponding Chern numbers are indicated for each band. (b) and (c) display the spin-wave modes at the Γ point for the lower and higher branch, respectively. (d) and (e) display a schematic top view of the spin-wave modes at the K point for the lower and higher branch, respectively.

the mutual degeneracy between the modes resulting in a band gap.

More specifically, the magnonic band gap is attributed to the NN Kitaev interactions and the out-of-plane component of the NNN DMI. The size of the latter, which is intrinsically present in CrI_3, is rather small ($|D^z_{ij}| = 0.03$ meV), also resulting in a small band gap. However, external tuning that breaks the inversion symmetry, e.g., the presence of a substrate, electric gating, or (nonuniform) strain, might induce additional DMI that could potentially increase the size of the band gap. In fact, by (artificially) increasing the DMI in our simulations, we verified that the band gap can be "tuned." As shown in Sec. SV of the Supplemental Material [33], the band gap scales almost linearly with the NNN DMI when all the other parameters are kept constant. Tuning the magnonic band gap in 2D materials under external stimuli poses an interesting direction for future research, as the size of the band gap can influence other material properties such as the magnon Hall conductivity. However, note that increasing the DMI may lead to noncollinear magnetization textures, e.g., spin cycloids or magnetic skyrmions, which will fundamentally change the magnonic behavior in the material [48,49]. Moreover, when the DMI is set to zero in our calculations, the band gap does not fully vanish, suggesting that there is a second mechanism at work, which we identify to be the Kitaev interaction between NN spins. In Sec. SV of the Supplemental Material [33], we show that one can tune the band gap by artificially changing K_{ij}, and we present a phase diagram showing how both the size and topology of the band gap vary as a function of D^z_{NNN} and K_{NN}. However, one should bear in mind that varying the strength of the Kitaev interaction also influences the overall shape of the dispersion, whereas changing the DMI mainly influences the dispersion around the K point.

C. Topology

Nontrivial band topology arises only in systems where nonzero Chern numbers predict the existence of edge states. The Chern number is a topological invariant with an integer value that is defined for the nth band as

$$\mathcal{C}_n = \frac{1}{2\pi i}\int_{\mathrm{BZ}} \Omega_{n\mathbf{k}}\, d^2k, \tag{4}$$

in which the Berry curvature can be calculated as

$$\Omega_{n\mathbf{k}} = i\sum_{n'\neq n} \frac{\langle n|\partial_{\mathbf{k}}\hat{\mathcal{H}}_{\mathbf{k}}|n'\rangle\langle n'|\partial_{\mathbf{k}}\hat{\mathcal{H}}_{\mathbf{k}}|n\rangle}{(\lambda_{n\mathbf{k}} - \lambda_{n'\mathbf{k}})^2}, \tag{5}$$

with $\lambda_{n\mathbf{k}}$ and $|n\rangle$ being the eigenvalues and eigenvectors, respectively, of the Heisenberg Hamiltonian $\hat{\mathcal{H}}_{\mathbf{k}}$ in reciprocal space. For systems that are gapless or show a trivial band gap, the Chern numbers vanish. In this paper, we calculate Chern numbers according to the link-variable method detailed in Ref. [50] for a discretized Brillouin zone (BZ). Applying this approach to the magnonic dispersion of monolayer CrI_3, we find Chern numbers of $\mathcal{C}_n = \pm 1$ for the upper and lower band, respectively, as shown in Fig. 2, classifying the material as a TMI with a nontrivial topological band gap. We attribute the origin of the topology to the breaking of time-reversal symmetry due to the spontaneous magnetization of CrI_3 [51]. Thus we can conclude that the topological nature of the bands persists in monolayer CrI_3, albeit with a significantly smaller band gap compared with bulk CrI_3 [9].

IV. BILAYER

A. Crystal structure and magnetic parameters

Bilayer CrI_3 can be constructed by stacking two monolayers on top of each other in a commensurate manner. The three different stacking orders that we consider in this paper are shown in Fig. 1. In analogy to Sivadas *et al.* [52], we refer to those stacking orders as AB (rhombohedral), AB′ (monoclinic), and AA. The former two stackings correspond to the low-temperature and the high-temperature phases of CrI_3, respectively [53]. In the AB stacking, the layers are stacked in such a way as to place the chromium atoms in one layer above the void in the chromium honeycomb of the adjacent layer, analogously to a Bernal-stacked graphene bilayer [Figs. 1(b) and 1(f)]. The AB stacking can be transformed into an AB′ stacking by sliding one of the layers by a third of the lattice vector along the zigzag direction [Figs. 1(c) and 1(g)]. Alternatively, by sliding one of the AB-stacked layers by a third of the lattice vector along the armchair direction, we obtain an AA-stacked bilayer, in which each atom in the top layer is placed exactly above its bottom layer counterpart [Figs. 1(d) and 1(h)].

TABLE II. Summary of the most important structural and magnetic parameters in bilayer CrI_3, including the lattice constant a and interlayer distance d, the average exchange and Kitaev constants $\langle J_{ij}\rangle$ and $\langle K_{ij}\rangle$, the average size of the DMI vectors $\langle|\mathbf{D}_{ij}|\rangle$, the DFT energy difference between the bilayer with an AFM and a FM interlayer ordering, and the average SIA.

	a (Å)	d (Å)	$\langle J_{\mathrm{NN}}\rangle$ (meV)	$\langle K_{\mathrm{NN}}\rangle$ (meV)	$\langle\lvert\mathbf{D}_{\mathrm{NN}}\rvert\rangle$ (meV)	$\langle J_{\mathrm{NNN}}\rangle$ (meV)	$\langle K_{\mathrm{NNN}}\rangle$ (meV)	$\langle\lvert\mathbf{D}_{\mathrm{NNN}}\rvert\rangle$ (meV)	$E_{\mathrm{AFM}}-E_{\mathrm{FM}}$ (meV)	$\langle\mathcal{A}_{ii}^{zz}\rangle$ (meV)
AB	6.915	3.400	−4.49	1.45	0.07	−0.62	0.13	0.03	12.13	−0.07
AB′	6.914	3.430	−4.49	1.45	0.07	−0.64	0.15	0.02	−0.06	−0.07
AA	6.908	3.505	−4.42	1.44	0.07	−0.65	0.15	0.03	0.84	−0.08

As shown in Table II, the different stacking orders show relatively similar lattice constants and interlayer distances. However, changes in interatomic distances and (super)superexchange bonding angles result in a different interlayer magnetic coupling, such that the AB and AA stackings prefer a FM ordering between the layers while the AB′ stacking slightly favors an AFM one. The latter is indicated in Table II by the DFT energy difference between AFM and FM phases. We found similar results in simulations using the Landau-Lifshitz-Gilbert (LLG) equation in SPIRIT [42] and the Metropolis Monte Carlo algorithm in SPINW [43]. In agreement with earlier theoretical work [52,54–56], we find that the overall ground state of the system is a FM-ordered AB-stacked bilayer. At first sight, the calculated FM ground state is at odds with experiment [2,57–60], where an AFM state is observed for even-layered CrI_3; however, recent work by Thiel *et al.* [57] suggests that the FM interlayer ordering might be the ground state for freestanding CrI_3, in agreement with most DFT studies, while encapsulation of CrI_3 causes a structural and magnetic phase transition to a state with an AFM interlayer ordering. In Sec. SII of the Supplemental Material [33], we discuss the stacking dependence of the interlayer ordering in more detail.

In Table II, we also summarize the predominant magnetic parameters for the CrI_3 bilayers calculated with the 4SM method. A full overview of all the calculated parameters for each specific pair can be found in Sec. SIV of the Supplemental Material [33]. For all stacking orders, the NN intralayer exchange interaction is anisotropic and strongly FM. This anisotropy, together with the SIA, causes the spins to prefer an out-of-plane orientation. Due to the rotational symmetry in the AB and AA stackings, the SIA matrix is reduced to only one parameter $\mathcal{A}_{ii}^{zz}$. In the AB′-stacked bilayer, this symmetry is absent requiring a calculation of the full SIA matrix; however, $\mathcal{A}_{ii}^{zz}$ will still be the dominant parameter, as most of the other matrix elements are very small or vanish.

To quantify the interlayer coupling, we calculated the interlayer NN and NNN exchange matrices for all stackings. For the AB′ stacking, we also calculate the 3NN interlayer exchange; for the other stackings this contribution is negligible as is demonstrated in Sec. SIV of the Supplemental Material [33]. In the AB- and AA-stacked bilayers, all NN and NNN interlayer exchange interactions are FM. However, the exchange parameters for the AB stacking are significantly stronger than for the AA stacking, resulting in a stronger preference for a FM ordering. In contrast, for the AB′-stacked bilayer, there is a competition between the NN exchange, which is FM, and the NNN and 3NN exchange interactions, which are AFM. Overall, this results in a weak AFM interlayer ordering, which is in agreement with earlier theoretical and experimental studies [2,52,54–61].

Interestingly, the sublattice symmetry is broken in the AB and AB′ stackings, leading to a difference in out-of-plane exchange interactions $\Delta J^{zz} = |J_{\mathrm{A}}^{zz} - J_{\mathrm{B}}^{zz}|$ between sublattices A and B of 0.92 meV for the AB stacking and 0.04 meV for the AB′ stacking. Note that J_{A}^{zz} and J_{B}^{zz} are the sum of the out-of-plane exchange components of all interacting spin pairs in a unit cell. The difference ΔJ^{zz} is substantial for the AB stacking because one sublattice has six stronger interlayer NNN interactions while the other sublattice has one weaker interlayer NN coupling and only three interlayer NNN interactions. For the AA stacking, there is no exchange difference since the sublattice symmetry is preserved.

The intralayer Kitaev constants in the bilayers are similar in size compared with the monolayer. For the AB and AB′ stacking, the NN Kitaev interaction is anisotropic, leading to different values for each bond, which is attributed to symmetry breaking due to the stacking. Since the NN Kitaev interaction is much stronger than the NNN and the interlayer ones, it is the only contribution having a significant influence on the spin-wave dispersion.

Unlike the monolayer system, the NN intralayer DMI is now nonzero and originates from the inversion symmetry breaking due to stacking. Similarly to the monolayer case, a nonzero NNN DMI arises. In all stackings, the interlayer DMI will be very small or completely absent, having a limited influence on the dispersion.

B. Spin-wave dispersion of bilayers with FM interlayer order

Using the magnetic parameters calculated with the 4SM method, we compute the spin-wave dispersion for the three stacking orders considered in this paper. In Fig. 3, we display the results for bilayer CrI_3 with different stackings, all with the FM interlayer ordering. In a bilayer, the unit cell contains four magnetic atoms, leading to four branches in the dispersion, two "acoustic" and two "optical" ones. The corresponding spin-wave modes at the Γ point of each branch are indicated in Fig. 3(d). The energy difference between these different modes is proportional to the strength of the interlayer coupling, hence the large separation for the AB stacking.

Each stacking shows a Goldstone gap at the Γ point, signaling that FM order is stable in each of them at finite temperatures. The gaps have sizes of $\Delta_\Gamma = 0.44$ meV, $\Delta_\Gamma = 0.34$ meV, and $\Delta_\Gamma = 0.35$ meV for the AB, AB′, and AA stackings, respectively. In the AB and AA stackings, we observe direct magnonic band gaps close to the K point of $\Delta_{K^*} = 0.37$ meV and $\Delta_K = 0.07$ meV, respectively. Similarly to the monolayer, we attribute the origin of these gaps to a

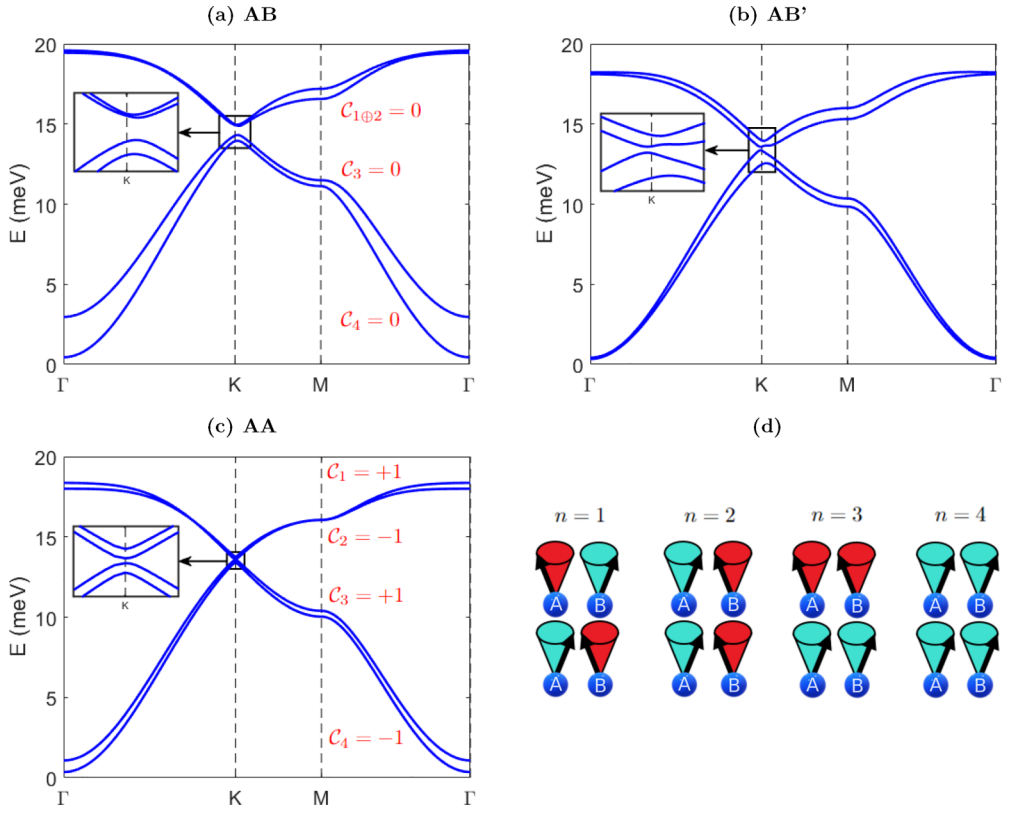

FIG. 3. Spin-wave dispersion for bilayer CrI_3 with a FM interlayer ordering in different stacking configurations. (a), (b), and (c) Spin-wave dispersion along the high-symmetry directions of the first Brillouin zone for the AB-, AB′-, and AA-stacked bilayers, respectively, with a FM interlayer ordering. In the AB and AA stackings, a direct magnonic band gap opens close to the K point. In the AB′ stacking, there is an indirect band crossing. Corresponding Chern numbers are indicated for single bands, and composite Chern numbers are indicated for degenerate bands. (d) schematically displays the corresponding spin-wave modes at the Γ point for each band.

combination of NNN DMI and NN Kitaev interactions. In the AB′ stacking, there is an indirect band crossing, as is often seen in semimetals, and thus no band gap. Notice that the band gaps do not occur exactly at $\mathbf{K}$ but are shifted to $\mathbf{K}^*$ due to the breaking of in-plane honeycomb symmetry caused by the interlayer coupling [29]. For the AB stacking we see a shift of $\mathbf{K} - \mathbf{K}^* = (-0.005, 0.021)\frac{2\pi}{a}$. In the AB′ stacking, we see shifts of $(0.037, -0.019)\frac{2\pi}{a}$ and $(0.008, -0.005)\frac{2\pi}{a}$ for the $n = 2$ and $n = 3$ bands, respectively. In the AA stacking, there is no shift. The first Brillouin zone contains two inequivalent high-symmetry points K and K' [Fig. 1(i)]. In the AB and AB′ stackings, where the sublattice symmetry is broken, we see a different behavior of the dispersion at each point. In the former, a band gap of only 0.05 meV opens close to the K' point (compared with $\Delta_{K^*} = 0.37$ meV). In both the AB and AB′ stackings, we see shifts from the the K' point to the K'^* point of roughly the same size but in the opposite direction. In the AA-stacked bilayer, the sublattice symmetry is preserved, resulting in exactly the same dispersion at both the K and K' points.

C. Spin-wave dispersion of bilayers with AFM interlayer order

By comparing the dispersion of the bilayers with FM interlayer ordering with the dispersion of the bilayers with AFM interlayer ordering (Fig. 4), it becomes clear that there is a strong dependence of the magnonic properties of CrI_3 on the interlayer ordering. First and foremost, notice that for the AA and AB stackings, there is a region close to the Γ point where the acoustic branches are zeroed. Consequently, there is no gap at the Γ point, and the integral in Eq. (3) will diverge, signaling that AFM order is unstable in these stackings at nonzero temperatures. However, in the AB′ stacking, there is a gap of $\Delta_\Gamma = 0.30$ meV, meaning that AFM order is stable in the monoclinic phase, which is in agreement with experimental observations [2,53,57–60]. Furthermore, also notice that, in contrast to the FM-ordered bilayers, we see a degeneracy of the two acoustic branches and the two optical branches. Only at the K point are there notable energy differences between the bands.

The dispersions of the bilayers with AFM interlayer order are characterized by band gaps of $\Delta_{K^*} = 1.04$ meV and $\Delta_{K'^*} = 0.97$ meV for the AB stacking, with shifts of $(\mathbf{K} - \mathbf{K}^*) = -(\mathbf{K}' - \mathbf{K}'^*) = (-0.005, 0.009)\frac{2\pi}{a}$, and by band gaps of $\Delta_{K^*} = \Delta_{K'^*} = 0.11$ meV for the AB′ stacking, with shifts of $(\mathbf{K} - \mathbf{K}^*) = -(\mathbf{K}' - \mathbf{K}'^*) = (-0.005, -0.008)\frac{2\pi}{a}$. At the K and K' points in the AA-stacking case, there is no band gap, but instead one finds a Dirac cone combined with two anticrossing branches.

D. Topology

When two or more bands are degenerate, crossing or touching, it is no longer possible to assign individual Chern numbers to each band. Instead, we define a composite Chern

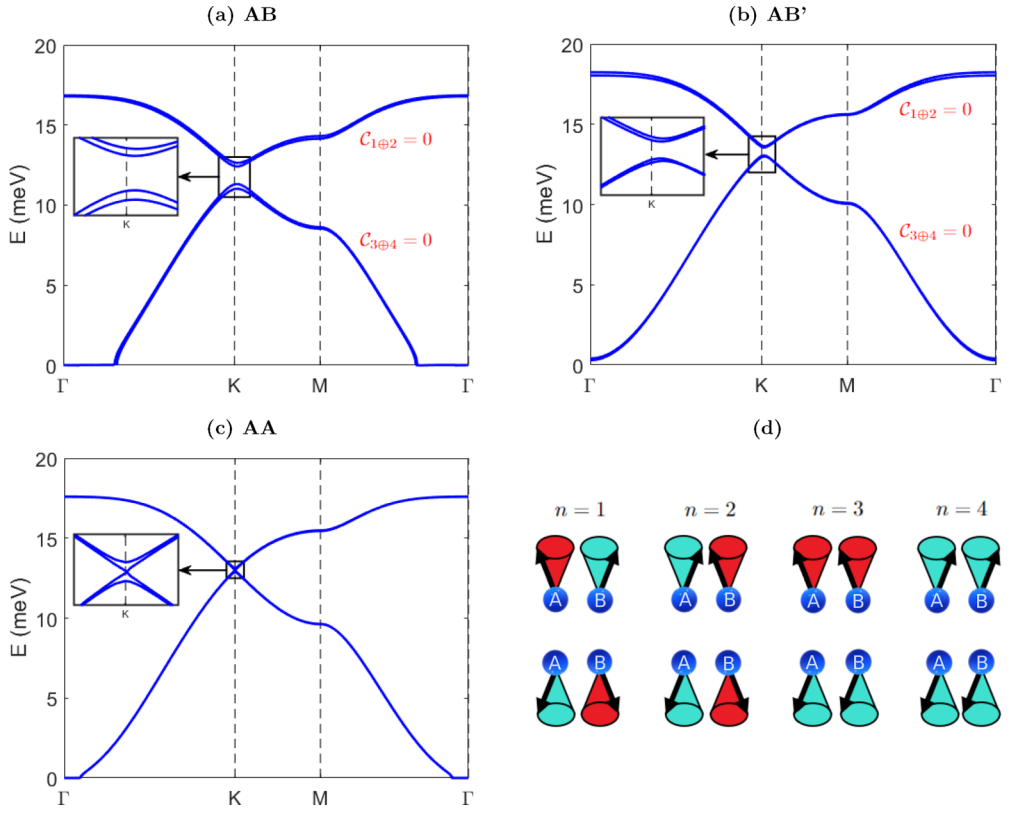

FIG. 4. Spin-wave dispersion for bilayer CrI_3 with an AFM interlayer ordering in different stacking configurations. (a), (b), and (c) Spin-wave dispersion along the high-symmetry directions of the first Brillouin zone for the AB-, AB′-, and AA-stacked bilayers, respectively, with an AFM interlayer ordering. In the AB and AB′ stackings a direct magnonic band gap opens close to the K point; meanwhile in the AA-stacked bilayer we observe a Dirac point. Corresponding composite Chern numbers are indicated for the bands and are all equal to zero. (d) schematically displays the corresponding spin-wave modes at the Γ point for each band.

number $\mathcal{C}_{n\oplus n'}$, jointly shared by the degenerate bands, and calculated as detailed in Ref. [62].

As shown in Fig. 3, there is a strong dependence of the Chern number on the stacking configuration in the FM-ordered bilayers. Although we are expecting a nontrivial topology of the band gaps in the FM bilayers, caused by the breaking of time-reversal symmetry due to the spontaneous magnetization, only the AA stacking shows nonzero Chern numbers. Thus the AA-stacked CrI_3 bilayer can be classified as a TMI. In the AB′ stacking there is no band gap; hence the Chern number is undefined, and the bands are not topological. In the AB stacking, all Chern numbers are equal to zero, meaning that the band gap is of trivial nature. We attribute the lack of topology in the latter stacking to the exchange difference ΔJ^{zz}, caused by the breaking of sublattice symmetry, which is very large for the AB stacking. In Sec. SV of the Supplemental Material [33], we show that by artificially reducing ΔJ^{zz} in our simulations, which also decreases the size of the band gap at the K point and the K' point, we can induce a topological phase transition to a state with nonzero Chern numbers of $\mathcal{C}_{1\oplus2} = +1$, $\mathcal{C}_3 = -1$, and $\mathcal{C}_4 = 0$, which confirms the influence that sublattice symmetry can have on the topology of magnonic bands [20].

In bilayers with AFM interlayer order, the bands are two-by-two degenerate, meaning that one can only define composite Chern numbers. In the case of AA stacking, there is no band gap; thus the Chern number is undefined, and the bands display no topological behavior. The composite Chern numbers for the other two stackings turn out to be zero for all considered bands, which can be related to the conservation of effective time-reversal symmetry in AFM materials, as the layers are time-reversed copies of each other [51]. However, in the next section, we will show that breaking this symmetry by an applied magnetic field leads to emergent topological states with nonzero Chern numbers.

E. Effect of an external magnetic field

In this section, we explore whether the magnonic dispersion and band topology of bilayer CrI_3 can be tuned by applying an out-of-plane external magnetic field.

In the case of a monolayer or the bilayers with FM interlayer order, there is only a trivial effect due to an applied magnetic field. Namely, the whole dispersion will uniformly shift up or down depending on the orientation of the applied field with respect to the magnetization. Notice that a very large, oppositely oriented field can flip the magnetization, which changes the sign of the Chern number of each band, meaning that the propagation direction of the magnonic edge states reverses.

In contrast, for bilayers with AFM interlayer order, an external magnetic field will lift the degeneracy between branches, shifting two branches up and two branches down in energy, and leading to additional interesting features in the

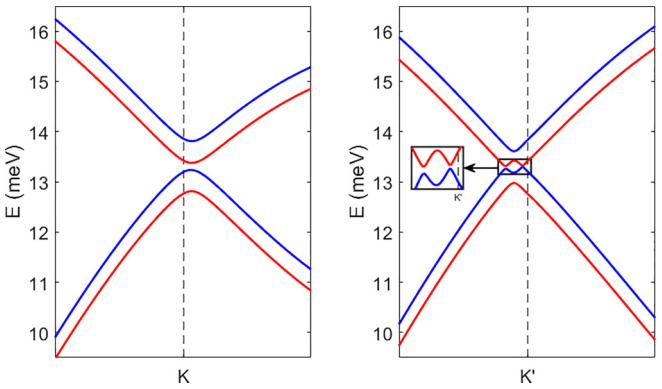

FIG. 5. Spin-wave dispersion for an AB′-stacked CrI_3 bilayer with an AFM interlayer ordering under the influence of an external magnetic field. The left and right panels compare the dispersion near the K point and that near the K' point, respectively, for an applied magnetic field of $B = 1.9$ T. Under the influence of the magnetic field, blue bands have shifted up and red bands have shifted down in energy.

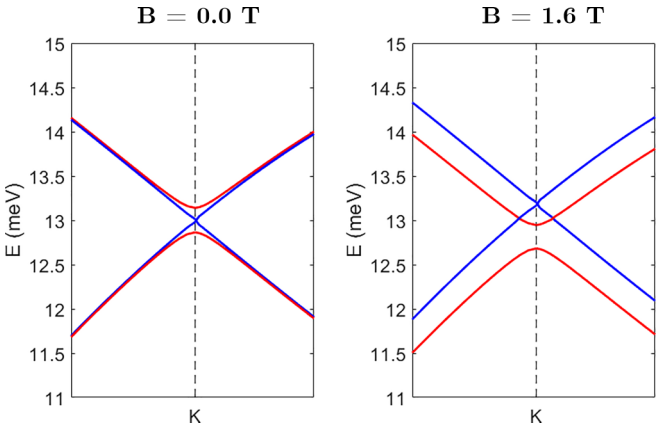

FIG. 6. Spin-wave dispersion for an AA-stacked CrI_3 bilayer with an AFM interlayer ordering under the influence of an external magnetic field. The left and right panels compare the dispersion at the K point for applied fields of $B = 0$ T and $B = 1.6$ T, respectively. Under the influence of the magnetic field, blue bands have shifted up and red bands have shifted down in energy, forming magnon nodal lines at the crossing points of the red and blue curves.

dispersion. Similar band shifts were observed by Cenker *et al.* [4], who reported the splitting of degenerate Raman peaks in the optical branches of an AFM-ordered monoclinic CrI_3 bilayer, after applying an external magnetic field. However, note that applying a magnetic field to AFM-ordered bilayers should be done carefully, as the interlayer magnetic state will switch to the FM one for sufficiently strong fields. Here, we calculate the spin-wave dispersion for the different stacking scenarios under sufficiently small applied field, where AFM interlayer order is safely stable (see Sec. SIII of the Supplemental Material [33]). The AFM-AB phase is very sensitive and changes into a FM interlayer order even for very weak applied field; hence it is excluded from our calculations in this section.

In the case of an AB′ stacking, the size of the band gap will decrease after applying the magnetic field, reaching a minimum of 0.01 meV for a field of $B = 1.9$ T, as shown in Fig. 5. In the right panel, one sees that, as the bands approach each other, they do not entirely touch or cross; instead we observe band inversion combined with a small band gap. Band inversion is an effect often also present in electronic topological insulators [63] and is typically caused by the SOC. For fields applied in the opposite direction, we see analogous behavior, as now the other two bands are shifted upwards and the previous two are shifted downwards. For fields larger than $B = 1.9$ T, the AFM interlayer ordering changes to a FM one (see Sec. SIII of the Supplemental Material [33]).

In Fig. 6, we show the influence of an external magnetic field with a magnitude of $B = 1.6$ T on the dispersion of an AFM-ordered AA-stacked CrI_3 bilayer. Applying the field shifts the Dirac node upwards or downwards depending on the polarity of the field, which leads to the formation of a closed Dirac magnon nodal-line loop at the crossover point of the red and blue bands in Fig. 6. The latter is a closed one-dimensional loop around the K point where two bands cross, exactly analogous to the nodal lines described for Dirac semimetals [64]. Decreasing the field leads to a smaller shift of the branches, resulting in nodal-line loops with a smaller radius. For fields larger than 1.6 T, the AFM interlayer ordering changes to a FM one (see Sec. SIII of the Supplemental Material [33]).

As mentioned earlier, in the absence of an applied field, all AFM bands show composite Chern numbers equal to zero, meaning that the band gaps have a trivial topology. Interestingly, after applying the magnetic field on the AB′-stacked bilayer, nonzero Chern numbers emerge as $\mathcal{C}_{1,4} = +1$ and $\mathcal{C}_{2,3} = -1$. In other words, by applying a magnetic field, which breaks the effective time-reversal symmetry of the material, a topological phase transition can be induced. In contrast, for the AA stacking, the (composite) Chern numbers remain undefined after applying the magnetic field, as the Dirac cone stays present.

V. CONCLUSIONS

We characterized the magnonic dispersion for intrinsically ferromagnetic monolayer and bilayer CrI_3 using linear spin-wave theory combined with a Heisenberg model parametrized from first principles. We showed that the monolayer is characterized by a small Dirac gap in the spin-wave dispersion, sourced to a specific combination of next-nearest-neighbor (NNN) DMI and nearest-neighbor Kitaev interactions. Nonzero Chern numbers are associated with the bands, indicating the topological nature of the band gap and suggesting that monolayer CrI_3 is a topological magnon insulator (TMI). In bilayer CrI_3, still with dominantly ferromagnetic intralayer interactions, we demonstrated a dependence of the dispersion on the geometric stacking order and the interlayer magnetic ordering, opening a band gap for the AB stacking (for both FM and AFM interlayer order), the AB′ stacking (only AFM), and the AA stacking (only FM); meanwhile the FM-ordered AB′ stacking shows an indirect band crossing, and the AFM-ordered AA stacking exhibits a Dirac point. Similarly to the monolayer case, we identified the DMI and Kitaev interactions as the leading causes behind

the opening of the band gap, both being modulated by the stacking order. The latter contradicts earlier work on bulk CrI_3 which claimed that only the NNN DMI, and, thus, not the Kitaev interaction, lies at the origin of the Dirac gap [9]. Interestingly, we found that the Chern number, and consequently the magnonic band topology, depends on the stacking configuration and the interlayer magnetic order, vanishing for all studied cases except in the FM-ordered AA bilayer. Thus, depending on the stacking order and the interlayer magnetic order, bilayer CrI_3 is classified as either a *topological* magnon insulator, a *trivial* magnon insulator, or a *magnon Dirac material*. Finally, we showed that the dispersion of the bilayers with AFM interlayer order can be tuned by an external out-of-plane magnetic field, changing both the size and the topology of the band gap for the AB′-stacked bilayer and introducing closed nodal-line loops in the dispersion of the AA bilayer.

The here-demonstrated presence of tunable band gaps of possibly topological nature in bilayer CrI_3 recommends it as a TMI that can serve as a platform to investigate tunable magnon Hall and spin Nernst effects in 2D. Our results could be verified experimentally by investigating the thermal magnon Hall effect in monolayer and bilayer CrI_3. Both the DMI and Kitaev interactions originate from the spin-orbit coupling, which is relatively strong in CrI_3 and thus lies at the origin of the topological band gap. If one wants to achieve a gapless spin-wave dispersion, we suggest looking at 2D magnets with a weaker SOC, e.g., $CrBr_3$ or $CrCl_3$, which are good candidates to host a Dirac point in the monolayer limit. In order to further tailor the magnonic band gap, one can induce and tune the DMI in CrI_3, or other 2D magnets, by external stimuli such as gating, (nonuniform) strain, heterostructuring, etc. Furthermore, our work demonstrates that stacking vdW monolayers, be it in regular bilayers or, in future work, multilayers and (moiré) heterostructures, poses a viable route to achieve broadly tunable magnonic properties in 2D materials and van der Waals homo- and heterostructures.

ACKNOWLEDGMENTS

The authors thank D. Šabani, B. Jorissen, and M. Shafiei for useful discussions. This work was supported by the Research Foundation–Flanders (FWO-Vlaanderen Grant No. 11O1423N) and the Special Research Funds of the University of Antwerp (BOF-UA). The computational resources used in this work were provided by the VSC (Flemish Supercomputer Center), funded by Research Foundation–Flanders (FWO) and the Flemish Government, Department EWI.

[1] M. Gibertini, M. Koperski, A. F. Morpurgo, and K. S. Novoselov, Nat. Nanotechnol. **14**, 408 (2019).
[2] B. Huang, G. Clark, E. Navarro-Moratalla, D. R. Klein, R. Cheng, K. L. Seyler, D. Zhong, E. Schmidgall, M. A. McGuire, D. H. Cobden, W. Yao, D. Xiao, P. Jarillo-Herrero, and X. Xu, Nature (London) **546**, 270 (2017).
[3] W. Jin, H. H. Kim, Z. Ye, S. Li, P. Rezaie, F. Diaz, S. Siddiq, E. Wauer, B. Yang, C. Li, S. Tian, K. Sun, H. Lei, A. W. Tsen, L. Zhao, and R. He, Nat. Commun. **9**, 5122 (2018).
[4] J. Cenker, B. Huang, N. Suri, P. Thijssen, A. Miller, T. Song, T. Taniguchi, K. Watanabe, M. A. McGuire, D. Xiao, and X. Xu, Nat. Phys. **17**, 20 (2021).
[5] R. M. Menezes, D. Šabani, C. Bacaksiz, C. C. de Souza Silva, and M. V. Milošević, 2D Mater. **9**, 025021 (2022).
[6] A. Barman, G. Gubbiotti, S. Ladak, A. O. Adeyeye, M. Krawczyk, J. Gräfe, C. Adelmann, S. Cotofana, A. Naeemi, V. I. Vasyuchka, B. Hillebrands, S. A. Nikitov, H. Yu, D. Grundler, A. V. Sadovnikov, A. A. Grachev, S. E. Sheshukova, J.-Y. Duquesne, M. Marangolo, G. Csaba *et al.*, J. Phys.: Condens. Matter **33**, 413001 (2021).
[7] Z. Cai, S. Bao, Z.-L. Gu, Y.-P. Gao, Z. Ma, Y. Shangguan, W. Si, Z.-Y. Dong, W. Wang, Y. Wu, D. Lin, J. Wang, K. Ran, S. Li, D. Adroja, X. Xi, S.-L. Yu, X. Wu, J.-X. Li, and J. Wen, Phys. Rev. B **104**, L020402 (2021).
[8] L. Chen, J.-H. Chung, B. Gao, T. Chen, M. B. Stone, A. I. Kolesnikov, Q. Huang, and P. Dai, Phys. Rev. X **8**, 041028 (2018).
[9] L. Chen, J.-H. Chung, M. B. Stone, A. I. Kolesnikov, B. Winn, V. O. Garlea, D. L. Abernathy, B. Gao, M. Augustin, E. J. G. Santos, and P. Dai, Phys. Rev. X **11**, 031047 (2021).
[10] F. Zhu, L. Zhang, X. Wang, F. J. dos Santos, J. Song, T. Mueller, K. Schmalzl, W. F. Schmidt, A. Ivanov, J. T. Park, J. Xu, J. Ma, S. Lounis, S. Blügel, Y. Mokrousov, Y. Su, and T. Brückel, Sci. Adv. **7**, eabi7532 (2021).
[11] I. Dzyaloshinsky, J. Phys. Chem. Solids **4**, 241 (1958).
[12] T. Moriya, Phys. Rev. **120**, 91 (1960).
[13] L. Chen, M. B. Stone, A. I. Kolesnikov, B. Winn, W. Shon, P. Dai, and J.-H. Chung, 2D Mater. **9**, 015006 (2022).
[14] J. A. Schneeloch, Y. Tao, Y. Cheng, L. Daemen, G. Xu, Q. Zhang, and D. Louca, npj Quantum Mater. **7**, 66 (2022).
[15] S. A. Owerre, J. Phys.: Condens. Matter **28**, 386001 (2016).
[16] S. A. Owerre, J. Appl. Phys. **120**, 043903 (2016).
[17] J. Fransson, A. M. Black-Schaffer, and A. V. Balatsky, Phys. Rev. B **94**, 075401 (2016).
[18] S. A. Owerre, J. Phys. Commun. **1**, 025007 (2017).
[19] S. S. Pershoguba, S. Banerjee, J. C. Lashley, J. Park, H. Ågren, G. Aeppli, and A. V. Balatsky, Phys. Rev. X **8**, 011010 (2018).
[20] H. Kim and S. K. Kim, Phys. Rev. B **106**, 104430 (2022).
[21] E. Aguilera, R. Jaeschke-Ubiergo, N. Vidal-Silva, L. E. F. F. Torres, and A. S. Nunez, Phys. Rev. B **102**, 024409 (2020).
[22] L.-C. Zhang, F. Zhu, D. Go, F. R. Lux, F. J. dos Santos, S. Lounis, Y. Su, S. Blügel, and Y. Mokrousov, Phys. Rev. B **103**, 134414 (2021).
[23] S. A. Owerre, Sci. Rep. **7**, 6931 (2017).
[24] S. A. Owerre, Phys. Rev. B **94**, 094405 (2016).
[25] H. Kondo, Y. Akagi, and H. Katsura, Phys. Rev. B **99**, 041110(R) (2019).
[26] A. T. Costa, D. L. R. Santos, N. M. R. Peres, and J. Fernández-Rossier, 2D Mater. **7**, 045031 (2020).
[27] T. Olsen, Phys. Rev. Lett. **127**, 166402 (2021).
[28] P. Delugas, O. Baseggio, I. Timrov, S. Baroni, and T. Gorni, arXiv:2105.04531.
[29] T. Gorni, O. Baseggio, P. Delugas, I. Timrov, and S. Baroni, arXiv:2212.09516.

[30] D. Šabani, C. Bacaksiz, and M. V. Milošević, Phys. Rev. B **102**, 014457 (2020).
[31] H. Xiang, C. Lee, H.-J. Koo, X. Gong, and M.-H. Whangbo, Dalton Trans. **42**, 823 (2013).
[32] C. Xu, J. Feng, H. Xiang, and L. Bellaiche, npj Comput. Mater. **4**, 57 (2018).
[33] See Supplemental Material at http://link.aps.org/supplemental/10.1103/PhysRevMaterials.7.024421 for additional tables, figures, and discussion of our results, which includes Refs. [2,22,30,34–42,44,52,54,55,57–60].
[34] G. Kresse and J. Hafner, Phys. Rev. B **47**, 558 (1993).
[35] G. Kresse and J. Furthmüller, Comput. Mater. Sci. **6**, 15 (1996).
[36] G. Kresse and J. Furthmüller, Phys. Rev. B **54**, 11169 (1996).
[37] P. E. Blöchl, Phys. Rev. B **50**, 17953 (1994).
[38] J. P. Perdew, K. Burke, and M. Ernzerhof, Phys. Rev. Lett. **77**, 3865 (1996).
[39] S. Grimme, J. Comput. Chem. **27**, 1787 (2006).
[40] S. Steiner, S. Khmelevskyi, M. Marsmann, and G. Kresse, Phys. Rev. B **93**, 224425 (2016).
[41] S. L. Dudarev, G. A. Botton, S. Y. Sevrasov, C. J. Humphreys, and A. P. Sutton, Phys. Rev. B **57**, 1505 (1998).
[42] G. P. Müller, M. Hoffmann, C. Dißelkamp, D. Schürhoff, S. Mavros, M. Sallermann, N. S. Kiselev, H. Jónsson, and S. Blügel, Phys. Rev. B **99**, 224414 (2019).
[43] S. Toth and B. Lake, J. Phys.: Condens. Matter **27**, 166002 (2015).
[44] K. Momma and F. Izumi, J. Appl. Crystallogr. **44**, 1272 (2011).
[45] J. L. Lado and J. Fernández-Rossier, 2D Mater. **4**, 035002 (2017).
[46] C. Bacaksiz, D. Šabani, R. M. Menezes, and M. V. Milošević, Phys. Rev. B **103**, 125418 (2021).
[47] N. D. Mermin and H. Wagner, Phys. Rev. Lett. **17**, 1133 (1966).
[48] F. Ma, Y. Zhou, H. B. Braun, and W. S. Lew, Nano Lett. **15**, 4029 (2015).
[49] T. Weber, D. M. Fobes, J. Waizner, P. Steffens, G. S. Tucker, M. Böhm, L. Beddrich, C. Franz, H. Gabold, R. Bewley, D. Voneshen, M. Skoulatos, R. Georgii, G. Ehlers, A. Bauer, C. Pfleiderer, P. Böni, M. Janoschek, and M. Garst, Science **375**, 1025 (2022).
[50] T. Fukui, Y. Hatsugai, and H. Suzuki, J. Phys. Soc. Jpn. **74**, 1674 (2005).
[51] P. A. McClarty, Annu. Rev. Condens. Matter Phys. **13**, 171 (2022).
[52] N. Sivadas, S. Okamoto, X. Xu, C. J. Fennie, and D. Xiao, Nano Lett. **18**, 7658 (2018).
[53] M. A. McGuire, H. Dixit, V. R. Cooper, and B. C. Sales, Chem. Mater. **27**, 612 (2015).
[54] S. W. Jang, M. Y. Jeong, H. Yoon, S. Ryee, and M. J. Han, Phys. Rev. Mater. **3**, 031001(R) (2019).
[55] P. Jiang, C. Wang, D. Chen, Z. Zhong, Z. Yuan, Z.-Y. Lu, and W. Ji, Phys. Rev. B **99**, 144401 (2019).
[56] D. Soriano, C. Cardoso, and J. Fernández-Rossier, Solid State Commun. **299**, 113662 (2019).
[57] L. Thiel, Z. Wang, M. A. Tschudin, D. Rohner, I. Gutiérrez-Lezama, N. Ubrig, M. Gibertini, E. Giannini, A. F. Morpurgo, and P. Maletinsky, Science **364**, 973 (2019).
[58] T. Song, Z. Fei, M. Yankowitz, Z. Lin, Q. Jiang, K. Hwangbo, Q. Zhang, B. Sun, T. Taniguchi, K. Watanabe, M. A. McGuire, D. Graf, T. Cao, J.-H. Chu, D. H. Cobden, C. R. Dean, D. Xiao, and X. Xu, Nat. Mater. **18**, 1298 (2019).
[59] T. Li, S. Jiang, N. Sivadas, Z. Wang, Y. Xu, D. Weber, J. E. Goldberger, K. Watanabe, T. Taniguchi, C. J. Fennie, K. F. Mak, and J. Shan, Nat. Mater. **18**, 1303 (2019).
[60] W. Chen, Z. Sun, Z. Wang, L. Gu, X. Xu, S. Wu, and C. Gao, Science **366**, 983 (2019).
[61] Y. Jiang, Y. Guo, X. Yan, H. Zeng, L. Lin, and X. Mou, Nanomaterials **11**, 2509 (2021).
[62] R. Zhao, G.-D. Xie, M. L. N. Chen, Z. Lan, Z. Huang, and W. E. I. Sha, Opt. Express **28**, 4638 (2020).
[63] Z. Zhu, Y. Cheng, and U. Schwingenschlögl, Phys. Rev. B **85**, 235401 (2012).
[64] T. O. Wehling, A. M. Black-Schaffer, and A. V. Balatsky, Adv. Phys. **63**, 1 (2014).